The ASTRODEEP Frontier Fields catalogues

II. Photometric redshifts and rest frame properties in Abell-2744 and MACS-J0416[*]

M. Castellano[1], R. Amorín[1], E. Merlin[1], A. Fontana[1], R. J. McLure[2], E. Mármol-Queraltó[2], A. Mortlock[2], S. Parsa[2], J. S. Dunlop[2], D. Elbaz[3], I. Balestra[4], A. Boucaud[5,18], N. Bourne[2], K. Boutsia[1], G. Brammer[6], V. A. Bruce[2], F. Buitrago[2,14,15], P. Capak[7], N. Cappelluti[8], L. Ciesla[3], A. Comastri[8], F. Cullen[2], S. Derriere[9], S. M. Faber[10], E. Giallongo[1], A. Grazian[1], C. Grillo[11], A. Mercurio[12], M. J. Michałowski[2], M. Nonino[4], D. Paris[1], L. Pentericci[1], S. Pilo[1], P. Rosati[13], P. Santini[1], C. Schreiber[3], X. Shu[3,16], and T. Wang[3,17]

1 INAF–Osservatorio Astronomico di Roma, via Frascati 33, 00040 Monte Porzio Catone (RM), Italy
  e-mail: marco.castellano@oa-roma.inaf.it
2 SUPA, Institute for Astronomy, University of Edinburgh, Royal Observatory, Edinburgh, EH9 3HJ, UK
3 Laboratoire AIM-Paris-Saclay, CEA/DSM/Irfu – CNRS – Université Paris Diderot, CEA-Saclay, pt courrier 131,
  91191 Gif-sur-Yvette, France
4 INAF–Osservatorio Astronomico di Trieste, via G. B. Tiepolo 11, 34143 Trieste, Italy
5 Institut d'Astrophysique Spatiale, CNRS, UMR 8617, Univ. Paris-Sud, Université Paris-Saclay, IAS, Bât. 121, 91405 Orsay,
  France
6 Space Telescope Science Institute, 3700 San Martin Drive, Baltimore, MD 21218, USA
7 Spitzer Science Center, 314-6 Caltech, Pasadena, CA 91125, USA
8 INAF–Osservatorio Astronomico di Bologna, via Ranzani 1, 40127 Bologna, Italy
9 Observatoire astronomique de Strasbourg, Université de Strasbourg, CNRS, UMR 7550, 11 rue de l'Université, 67000 Strasbourg,
  France
10 UCO/Lick Observatory, University of California, 1156 High Street, Santa Cruz, CA 95064, USA
11 Dark Cosmology Centre, Niels Bohr Institute, University of Copenhagen, Juliane Maries Vej 30, 2100 Copenhagen, Denmark
12 INAF–Osservatorio Astronomico di Capodimonte, via Moiariello 16, 80131 Napoli, Italy
13 Dipartimento di Fisica e Scienze della Terra, Università degli Studi di Ferrara, via Saragat 1, 44122 Ferrara, Italy
14 Instituto de Astrofísica e Ciências do Espaço, Universidade de Lisboa, OAL, Tapada da Ajuda, PT1349-018 Lisbon, Portugal
15 Departamento de Fìsica, Faculdade de Ciências, Universidade de Lisboa, Edifìcio C8, Campo Grande, PT1749-016 Lisbon,
  Portugal
16 Department of Physics, Anhui Normal University, Wuhu, 241000 Anhui, PR China
17 School of Astronomy and Astrophysics, Nanjing University, 210093 Nanjing, PR China
18 Sorbonne Universités, UPMC Univ. Paris 6 et CNRS, UMR 7095, Institut d'Astrophysique de Paris, 98bis Bd Arago, 75014 Paris,
  France

ABSTRACT

Aims. We present the first public release of photometric redshifts, galaxy rest frame properties and associated magnification values in the cluster and parallel pointings of the first two Frontier Fields, Abell-2744 and MACS-J0416. The released catalogues aim to provide a reference for future investigations of extragalactic populations in these legacy fields: from lensed high-redshift galaxies to cluster members themselves.
Methods. We exploit a multiwavelength catalogue, ranging from *Hubble* Space Telescope (HST) to ground-based *K* and *Spitzer* IRAC, which is specifically designed to enable detection and measurement of accurate fluxes in crowded cluster regions. The multiband information is used to derive photometric redshifts and physical properties of sources detected either in the *H*-band image alone, or from a stack of four WFC3 bands. To minimize systematics, median photometric redshifts are assembled from six different approaches to photo-*z* estimates. Their reliability is assessed through a comparison with available spectroscopic samples. State-of-the-art lensing models are used to derive magnification values on an object-by-object basis by taking into account sources positions and redshifts.
Results. We show that photometric redshifts reach a remarkable ∼3–5% accuracy. After accounting for magnification, the *H*-band number counts are found to be in agreement at bright magnitudes with number counts from the CANDELS fields, while extending the presently available samples to galaxies that, intrinsically, are as faint as $H \sim 32$–33, thanks to strong gravitational lensing. The Frontier Fields allow the galaxy stellar mass distribution to be probed, depending on magnification, at 0.5–1.5 dex lower masses with respect to extragalactic wide fields, including sources at $M_{\rm star} \sim 10^7$–10^8 $M_\odot$ at $z > 5$. Similarly, they allow the detection of objects with intrinsic star formation rates (SFRs) >1 dex lower than in the CANDELS fields reaching 0.1–1 $M_\odot$/yr at $z \sim 6$–10.

Key words. catalogs – galaxies: high-redshift – methods: data analysis – galaxies: distances and redshifts

1. Introduction

The use of photometric redshifts and spectral energy distribution (SED) fitting techniques is acquiring an ever increasing importance for investigating the properties of extragalactic populations where spectroscopic studies of large flux-limited samples are beyond the reach of current instrumentation. With this in mind, significant effort has been spent in assembling determinations of both photo-zs and galaxy rest-frame properties from available multiband datasets of deep field surveys, such as GOODS (Grazian et al. 2006), COSMOS (Ilbert et al. 2009), CANDELS (Dahlen et al. 2013) and 3D-HST (Skelton et al. 2014). The relevance of these analyses is well demonstrated by the emerging collaborative efforts, which combine different codes and techniques to smooth out possible systematics in the computation of robust photo-zs and rest-frame properties (e.g. Santini et al. 2015; Mobasher et al. 2015).

Accurate estimates of photometric redshifts and galaxy properties are, today, the missing ingredient for exploiting the Frontier Fields (FF) survey, an HST observing program that targets six galaxy cluster fields and six parallel "blank" fields at depths that are comparable to the *Hubble* Ultra Deep Field. Thanks to the magnification by the foreground galaxy clusters, the FF survey enables the detection of galaxies as intrinsically faint as future *James Webb* Space Telescope targets, while also reducing cosmic variance effects in the study of ultra-faint galaxy populations, as a result of the independent pointings. The FF survey promises to be a milestone in extragalactic studies in the years to come.

In this paper, we present a public release of photometric redshifts and rest-frame galaxy properties from multiwavelength photometry of the Frontier Fields, Abell-2744 (A2744 hereafter) and MACS-J0416 (M0416) cluster and parallel fields, that include both HST and deep K-band and *Spitzer* information. A detailed description of the dataset and photometric measurements is presented in a companion paper by Merlin et al. (2016, M16 hereafter). The multiband and photometric redshift catalogues of the FF have been developed in the context of the European FP7-Space project ASTRODEEP[1]. The structure of the paper is as follows: in Sect. 2 we briefly describe the available photometric and spectroscopic data and the catalogue assembly procedure from M16. Section 3 will introduce our procedure for estimating photometric redshifts and provide an evaluation of their accuracy. The determination of magnification values on an object-by-object basis and the resulting demagnified number counts are discussed in Sect. 4, while demagnified stellar masses and star formation rates (SFRs) are presented in Sect. 5. Finally a summary of the work is provided in Sect. 6, and a description of the publicly available dataset[2] is included in the Appendix.

Throughout the paper, observed and rest-frame magnitudes are in the AB system, and we adopt the Λ-CDM concordance model ($H_0 = 70$ km s^{-1} Mpc^{-1}, $\Omega_M = 0.3$, and $\Omega_\Lambda = 0.7$).

2. Multiwavelength catalogues

A detailed description of the dataset and of the catalogue assembly strategy is provided in M16; we summarise here the information that is most relevant for this paper.

2.1. Dataset

The A2744 and M0416 are the first two of a total of six twin fields observed by HST in parallel (i.e. the cluster pointing together with a "blank" parallel pointing), in three optical and four near-infrared bands: *F435W*, *F606W*, and *F814W* (ACS); *F105W*, *F125W*, *F140W*, and *F160W* (WFC3). The HST bands have a typical 5σ depth in the range 28.5-29.0 AB in 2 PSF-FWHM apertures. Along with the seven HST bands, we include in each field the publicly available Hawk-I@VLT Ks images from ESO Programme 092.A-0472[3] ($\sim$26.2 at 5σ), and the IRAC 3.6 and 4.5 μm data acquired under DD time and, in the case of M0416, Cycle-8 program iCLASH (80168) ($\sim$25 AB at 5σ).

To fully exploit the depth of the images and to detect outshone faint sources, we developed a procedure to remove the foreground light of bright cluster sources and the intra-cluster light (ICL). We start with the H160 image applying the following procedure:

1) a first raw estimate of the ICL component is obtained by masking $S/N > 8$ pixels in the original H160 image and fitting the ICL light with Galfit (Peng et al. 2010), using one or more Ferrer profiles (see Giallongo et al. 2014). The best-fit model is then subtracted from the original image. 2) On the ICL-subtracted H160 image, we use Galapagos (Barden et al. 2012) to obtain a single Sérsic fit of the brightest cluster members, typically mag < 19 galaxies close to the cluster centre. 3) We then progressively refine the fit for these objects by adding a second, "bulgy" component and fitting again with Galfit, leaving the structural parameters of the galaxies free to adjust; if necessary, we iterate the procedure adding further components until a satisfying residual is obtained. 4) Having obtained the best fit for the galaxies, we keep them fixed and fit the ICL again with Galfit on the original image, leaving its parameters free to adjust; then we obtain a "final residual" image by subtracting this final ICL model and the bright galaxy models from the image. 5) Finally, we create a median-filtered version of the residual images over a 1×1 arcsec box. To avoid the affect of signals from faint objects, we exclude from the computation all pixels at >1σ above zero counts and their nearest neighbours. We obtain the final processed frame by subtracting the resulting median-filtered image from the "final residual" one, thus smoothing out local fluctuations and Galfit residuals and allowing for a more efficient detection.

We subtract ICL and bright sources from the other HST bands using the final fitting parameters of the nearest redder band as a first guess and simultaneously fitting all the components at once. Our catalogue is extracted by performing the detection on the final processed H160 image with SExtractor (Bertin & Arnouts 1996) using a customized version of the HOT+COLD approach (Galametz et al. 2013; Guo et al. 2013). The resulting 90% detection completeness limits for point sources and disk-like galaxies, as estimated using simulations, are at $H \sim 27.75$ and $H \sim 27.25$, respectively. We extract fluxes from the other HST bands with SExtractor in dual mode after having PSF-matched them to the H160 PSF through appropriate

---

convolution kernels derived from bright unsaturated stars. Total fluxes in the detection band are estimated from SExtractor `FLUX_AUTO`. Total fluxes in the other HST bands are computed by scaling the total flux in the detection band on the basis of the relevant isophotal colours that were computed from SExtractor `FLUX_ISO` values. K and IRAC photometry is obtained via a template-fitting technique with `T-PHOT` (Merlin et al. 2015) using galaxy shapes in the detection band as "prior" information. `T-PHOT` allows us to fit "real" sources together with analytical models; therefore we used the detected $H160$ catalogue plus the bright source models as priors. Before the fit, measurement images are processed, re-estimating the background and the rms via an injection of fake PSF-shaped sources in void regions. A local background subtraction is also performed during the fit, allowing for a better estimation of the flux for objects that fall within the halos of bright sources. All fluxes are corrected for galactic extinction that was derived from Schlegel et al. (1998) dust emission maps.

To include all faint sources of potential interest we also perform an additional detection using `SExtractor` with the same parameter set on a weighted average of the processed $Y105$, $J125$, $JH140$, and $H160$ images and derive photometry in the other bands in the same way as for the H-detected sample. The final list of detected sources comprises the main H-detected catalogue plus all those IR-detected ones whose segmentation does not overlap with any pixel that belong to H-detected objects according to the relevant segmentation maps. The final catalogues contain information on ten bands for 2596 (H-detected)+976 (IR-detected) sources in A2744-Cluster, 2325+1086 in A2744-Parallel, 2556+832 in M0416-Cluster, and 2581+1152 in M0416-Parallel.

2.2. Spectroscopic samples

We look for counterparts of our sources in available spectroscopic samples by performing a cross-correlation within 1 arcsec radius. We consider the following public datasets: Owers et al. (2011) (objects with quality flag $Q = 4$ or higher) and the arcs from Richard et al. (in prep.) for A2744; Ebeling et al. (2014), and the arcs from Grillo et al. (2015) and Christensen et al. (2012) for M0416. For both A2744 and M0416 clusters, we include redshifts with quality flag $Q = 3$ and $Q = 4$ from the Grism Lens-Amplified Survey from Space (GLASS; GO-13459; PI: Treu, Hoag et al., in prep.; Treu et al. 2015; Wang et al. 2015). Objects having a positive match with reliable public samples are assigned the measured spectroscopic redshift in our catalogues. To assess photo-z reliability, we also match our catalogues with the M0416 proprietary redshift from the CLASH-VLT survey (ESO Large Programme 186.A-0.798, PI: Rosati, Rosati et al. 2014; Balestra et al. 2016). The final samples include 86, 10, 194 public spectroscopic redshifts in A2744 cluster field, A2744 parallel field, and MACS0416 cluster field, respectively. No public spectroscopic redshifts are found in the MACS0416 parallel field. Thanks to the addition of the aforementioned proprietary data, we reach a total of 207 and 33 spectroscopically confirmed objects in the MACS0416 cluster and MACS0416 parallel fields, respectively.

3. Photometric redshifts

We measure photometric redshifts for all the sources in our catalogues with six different techniques: 1) `OAR`; 2) `McLure`; 3) `Mortlock`; 4) `Parsa`; 5) `Marmol-Queralto-1`;
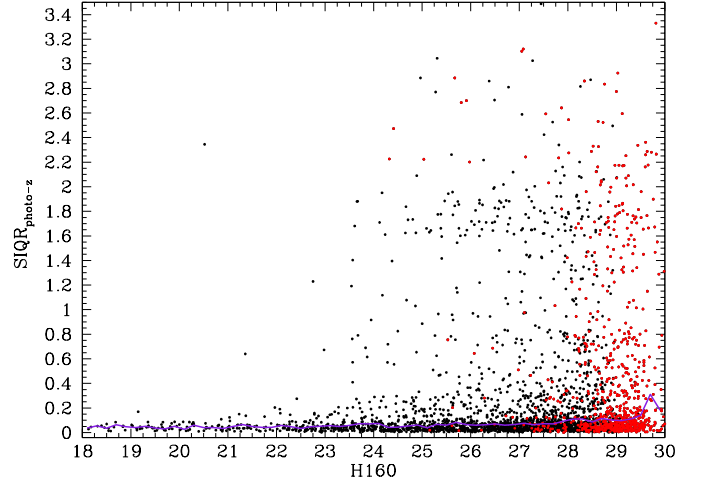

Fig. 1. Semi-interquartile range of the six different photo-z estimates as a function of the H-band magnitude (or upper limit) for H-detected (black circles) and IR-detected (red) sources in the A2744 cluster field. The median SIQR as a function of magnitude is shown as a purple line.

6) `Marmol-Queralto-2`. The `OAR` photometric redshifts are obtained with the `zphot.exe` code following the well-tested procedure described in Fontana et al. (2000) and Grazian et al. (2006; see also Dahlen et al. 2013; Santini et al. 2015). Best-fit photo-zs are obtained through a χ^2 minimization over the observed HST+IR bands using SED templates from `PEGASE` 2.0 (Fioc & Rocca-Volmerange 1997) at $0.0 < z < 10.0$. We set flux = 0 in place of negative values and a minimum allowed photometric uncertainty corresponding to 0.05 mag for the HST and Ks bands and to 0.1 mag for the IRAC bands: errors smaller than these values are replaced by the minimum allowed uncertainty. The `Parsa` and `Mortlock` runs both use the publicly available `Le Phare` code (Arnouts et al. 1999), and employ the `PEGASE` and zCOSMOS (Ilbert et al. 2006) template sets respectively. Both the `Marmol-Queralto` runs utilize the publicly available `EAZY` code (Brammer et al. 2008), and they employ the PCA (built following Blanton & Roweis 2007) and `PEGASE` template sets, respectively. The `McLure` run is based on his own proprietary code, as described in McLure et al. (2011), which employs Bruzual & Charlot (2003) templates. All of the photometric redshift runs, with the exception of the `OAR` applied adjustments to the photometric zeropoints and the `McLure`, `Parsa,` and `Mortlock` runs, included strong nebular emission lines in the SED fits. To minimize systematics owing to the use of a single approach, as reference photo-z for each object we set the median value from the six available estimates. In Fig. 1 we show the uncertainty (semi-interquartile range, SIQR) on the median photo-z, as a function of the observed H-band magnitude, for sources in the A2744 cluster field. Typical SIQR (purple line in Fig. 1) ranges from 0.05 at bright magnitudes to 0.3 for sources at $H > 29$. The percentage of sources with highly uncertain median photo-z (SIQR > 1) is below ~10% up to $H \sim 26.0$ and reaches ~20% at the faintest magnitudes. Similar results are found in the other fields under analysis.

Galaxy physical properties are then computed by fitting Bruzual & Charlot (2003 – BC03) templates with the `zphot.exe` code at the previously determined median photometric redshift. In the BC03 fit we assume exponentially declining star formation histories with e-folding time $0.1 \leq \tau \leq 15.0$, a Salpeter (1955) inital mass function, and we allow both Calzetti et al. (2000) and Small Magellanic Cloud (Prevot et al. 1984) extinction laws. Absorption by the inter-
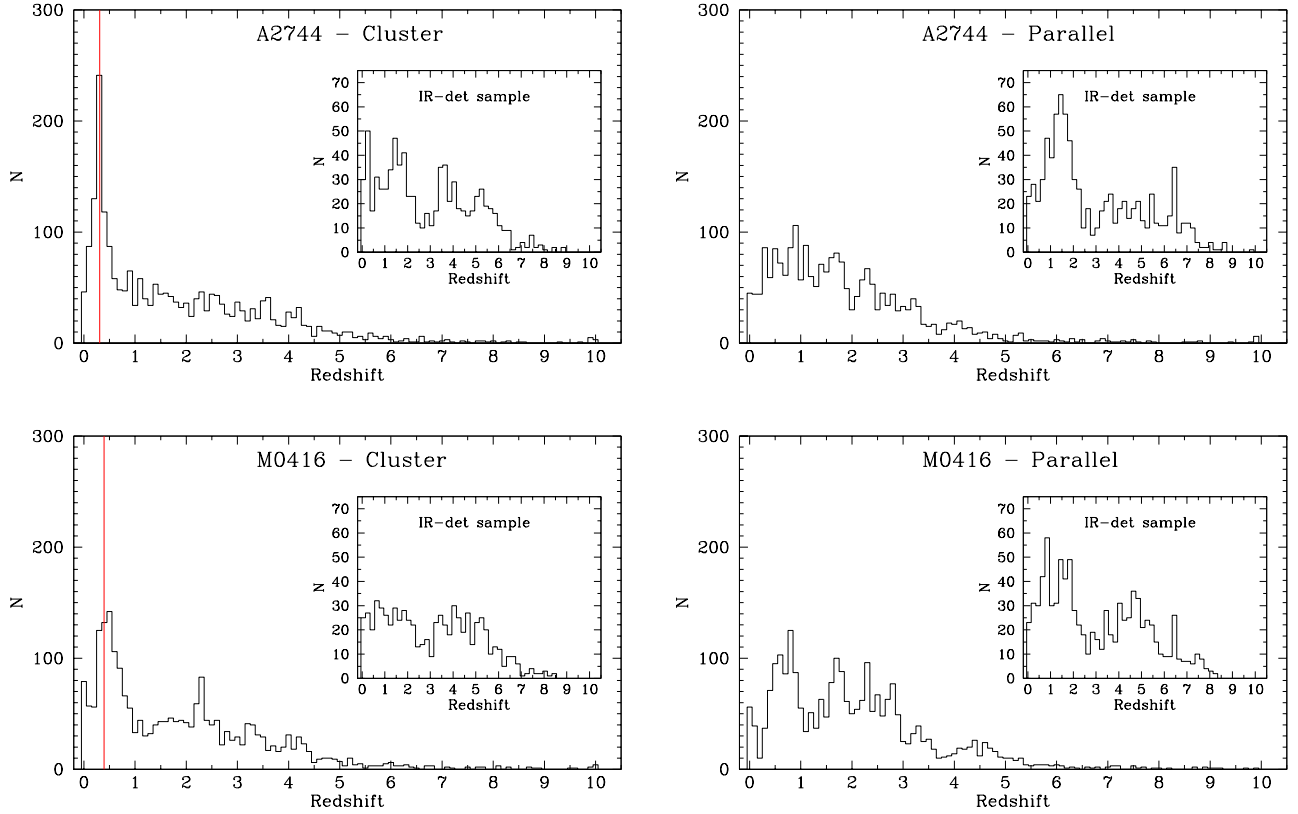
Fig. 2. Photometric redshift distribution of *H*-detected catalogues in, *from top to bottom, left to right*: A2744 Cluster, A2744 Parallel, M0416 Cluster, M0416 Parallel. *Inset plots* show the distribution of the additional IR-detected samples. Vertical red lines mark the redshift of the lensing clusters.

Table 1. Photometric redshift accuracy.

Field	Spec. sample	N. outliers (fraction)	$\langle \Delta z/(1+z) \rangle$	$\sigma_{\Delta z/(1+z)}$
A2744-Cl	54	4 (7.3%)	−0.0140	0.043
A2744-Par	9	0 (0%)	0.0004	0.056
M0416-Cl	155	10 (6.5%)	−0.0004	0.043
M0416-Par	33	3 (9%)	−0.0299	0.0362

galactic medium (IGM) is modelled following Fan et al. (2006). We consider the following range of physical parameters: $0.0 \leq E(B-V) \leq 1.1$, Age ≥ 10 Myr (defined as the onset of the star formation episode), metallicity $Z/Z_\odot = 0.02, 0.2, 1.0, 2.5$. We fit all the sources both with stellar emission templates only, and including the contribution from nebular continuum and line emission following Schaerer & de Barros (2009), assuming an escape fraction of ionizing photons $f_{esc} = 0.0$ (see also Castellano et al. 2014, for details).

Photometric redshifts and rest-frame properties are determined using all ten available bands with the following exceptions: 1) HST bands having `SExtractor FLAG` ≥ 16 and/or unphysical fluxes or uncertainties (typically truncated or problematic sources); 2) *K*-band and IRAC fluxes with a maximum covariance ratio `MaxCvRatio` ≥ 1.0 in the relevant `T-PHOT` extraction, indicating that the measurement is hardly reliable owing to severe blending with other sources (see Merlin et al. 2015). As a result, all ten bands are used in the fit for ~65% of the sources in the cluster pointings and for >90% in the blank fields. Most of the remaining objects are fit with HST+*K*s photometry while (for ~25% of the sources) one or both IRAC bands are excluded

owing to the large covariance. The resulting photometric redshift distributions in the four fields are shown in Fig. 2, and the comparisons between photometric and spectroscopic redshifts are shown in Fig. 3 for the two cluster pointings. The latter is computed only on the sources with reliable photometry, i.e. excluding areas subject to `Galfit` subtraction of bright sources and having at least five HST bands available for computing the photometric redshifts (`RELFLAG` = 1, see Appendix). Following Dahlen et al. (2013), we define as outliers all objects having $|\Delta z/(1 + z)| = |(z_{spec} - z_{phot})/(1 + z_{spec})| \geq 0.15$. In Table 1, we report the fraction of outliers along with average and rms of $\Delta z/(1 + z)$ that were computed on the remaining objects. Clearly, the limited number of spectroscopic sources and their redshift distribution do not allow for an in-depth evaluation of the accuracy of photometric redshifts in all fields. It is safe to take as reference the two cluster fields that have a larger spectroscopic sample, which also includes high-redshift lensed galaxies, where we consistently find an accuracy $\sigma_{\Delta z/(1+z)} \sim 0.04$ and ~7% of outliers. We verified that the median photometric redshifts are more accurate than the individual runs, when compared to spectroscopic redshifts. In the cluster fields the individual runs show
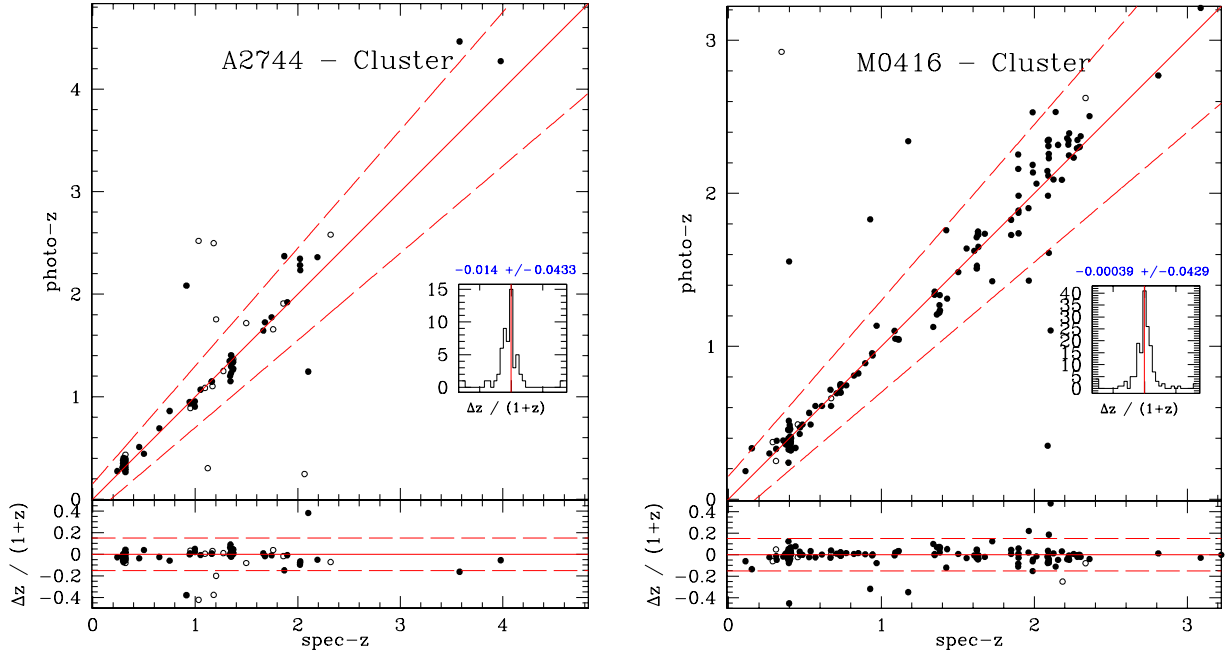
Fig. 3. Comparison between photometric and spectroscopic redshifts in the A2744 (*left*) and M0416 (*right*) clusters. Filled circles represent best quality spectroscopic redshifts used to compute the photometric redshift accuracy reported in Table 1, empty circles objects with "reliable" redshift from the GLASS sample (quality flag = 3). *Lower panels* show the $\Delta z/(1 + z_{spec}) = (z_{spec} - z_{phot})/(1 + z_{spec})$ as a function of z_{spec}. The *inset* in each of the *upper panels* presents the relevant distribution of $\Delta z/(1 + z_{spec})$ with its average and rms after excluding $|\Delta z/(1 + z_{spec})| > 0.15$ outliers, as discussed in the text. Red dashed lines in both panels enclose the $|\Delta z/(1 + z_{spec})| \leq 0.15$ region.

similar performances with $\sigma_{\Delta z/(1+z)} \sim 0.05-0.06$, $\langle \Delta z/(1 + z) \rangle \gtrsim 10^{-3}$ and 8–11% of outliers. The photometric redshift accuracy at the redshift of the clusters is comparable to the global one, implying that the redshifts presented here can be used to individuate non-spectroscopic cluster members (see also Fig. 7). However, we caution against a possible tendency for a luminosity-dependent behaviour of the photometric redshift offset in the M0416 cluster field, with likely cluster members at $H > 26$ having a typical offset $\Delta z = +0.05$, which appears at the origin of a broader and slightly shifted redshift peak in the relevant redshift distribution (bottom left panel of Fig. 2). The lack of spectroscopic coverage of these sources prevents a firm conclusion in this respect. Finally, we note that the typical photometric redshift accuracy in our Frontier Fields sample is poorer than the one achieved in the CANDELS fields (Dahlen et al. 2013), and comparable in terms of scatter and offset, but with a larger fraction of outliers, to photo-zs from the 16-band CLASH photometry (Jouvel et al. 2014). To constrain the origin of these differences, we tested the performance of one of our photo-z procedures (the OAR one) on the CANDELS GOODS-South catalogue, which we restricted to the same ten bands available for the FF and using the same SED libraries and fitting options as for the FF. The difference in depth among the FF and the GOODS fields is not a big concern here since spectroscopic samples mostly comprise high S/N sources in both cases, such that this test effectively constrains the accuracy of our procedure on the available FF bands compared to a run on the full dataset (the E-zphot method in Dahlen et al. 2013). We find 8% of outliers and a $\sigma_{\Delta z/(1+z)} = 0.045$, thus an accuracy comparable to the that reached in the FFs by the OAR procedure alone ($\sigma_{\Delta z/(1+z)} \sim 0.05$). On the full GOODS 19-bands catalogue, we found 4.1% of outliers and a $\sigma_{\Delta z/(1+z)} = 0.037$, suggesting that the lower number of bands available and narrower spectral coverage is the most relevant limiting factor in the accuracy of photometric redshifts in the Frontier Fields.

3.1. Comparison with previous works

A critical aspect of the Frontier Field campaign is the investigation of lensed, intrinsically faint star forming galaxies at very high redshifts. While the presently released catalogue is designed to a have broader use by providing data for robustly detected sources at any redshift, it is useful anyway to compare it with the available information on high-redshift samples in the fields under analysis. To this end, we cross-correlated our catalogues (adopting a matching radius of 2PSF-*FWHM* = 0.4 arcsec) with the samples in: Laporte et al. (2014), Zitrin et al. (2014; see also Oesch et al. 2015), Zheng et al. (2014), Atek et al. (2015), Coe et al. (2015) McLeod et al. (2015), Ishigaki et al. (2015). The most studied field is A2744 with a total sample made up of 74 Lyman-break galaxies (LBGs) at $z \gtrsim 5$. We find that 58 of these sources are present in our catalogues (of which 12 are from the additional IR-detected sample). A comparison between our photo-zs and those published for the A2744 cluster LBGs is shown in Fig. 4, which indicates a good consistency with respect to previous estimates. A similar result is found by making a comparison with the much smaller LBG samples from the M0416 fields (Laporte et al. 2015; Coe et al. 2015; McLeod et al. 2015) and from the A2744 parallel field (Ishigaki et al. 2015; McLeod et al. 2015). We inspected the 16 LBGs missing from our A2744 cluster catalogue and found that in three cases they are undetected, while 13 are very close to bright galaxies and are not deblended from them. These findings are easily explained on the basis of the detection strategy we adopted. Indeed, while the aforementioned works aim at an ultra-deep detection of small-size and faint high-redshift sources, our catalogues are based on a compromise between an aggressive detection, which is ideal for faint objects, and the capability of avoiding over-deblending of extended lower redshift sources. Nonetheless, the recovery of most of the previously found high-z candidates with comparable
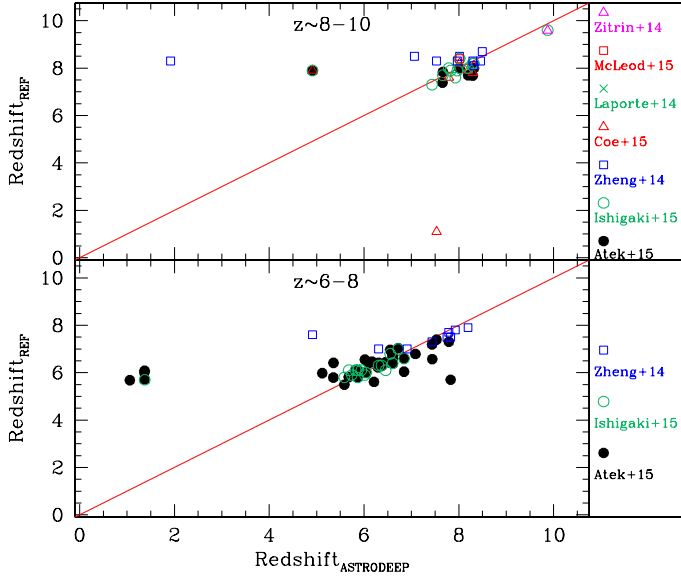
Fig. 4. Comparison between photometric redshifts from our catalogues and those from previous papers on high-redshift LBG samples.

photo-z estimate highlights that the general-purpose catalogues that are presented here are effective across a wide redshift range.

We also compared our photometric redshift catalogue for the M0416 cluster with the one[4] made available by the CLASH collaboration (Postman et al. 2011). The comparison performed on objects with robust cross-correlation between the two samples (1 match within 0.2 arcsec) is shown in Fig. 5. We separately consider bright objects with a highly-reliable photo-z in the CLASH catalogue according to the parameters released by the developers: $\chi^2 \leq 1$ and a high ODDS value (we set >0.8), indicating a sharply peaked unimodal redshift likelihood distribution. The agreement is remarkable, with the exception of a small number of sources having $z_{\rm phot} \lesssim 0.8$ in our catalogue and $z_{\rm phot} \sim 4$ in the CLASH one. We looked at their position in the $z \sim 4$ colour selection diagram from Castellano et al. (2012) (bottom panel in Fig. 5), finding that their colours are indeed typical of low-redshift galaxies excluded from the B-dropout selection window. While this is true when both our photometric catalogue and the CLASH one are compared, the flux uncertainty and scatter is significantly larger in the latter case, which further highlights the improvementes enabled by the depth of the FF dataset and, possibly, by our catalogue-building procedure, which includes the accurate subtraction of the foreground bright galaxies and ICL emission.

4. Demagnified number counts

We use available lensing models of the two FF fields to assign magnification values to sources in our catalogues. Five of the models under consideration assume that cluster galaxies trace the cluster mass substructure: the CATS (P.I. Ebeling, e.g. Jauzac et al. 2014) and Sharon (e.g. Johnson et al. 2014) models, based on Lenstool, the GLAFIC model (Oguri 2010; Ishigaki et al. 2015), and the two different parametrizations (LTM and NFW) provided by the Zitrin team (e.g. Zitrin et al. 2013). The three remaining models that were provided by
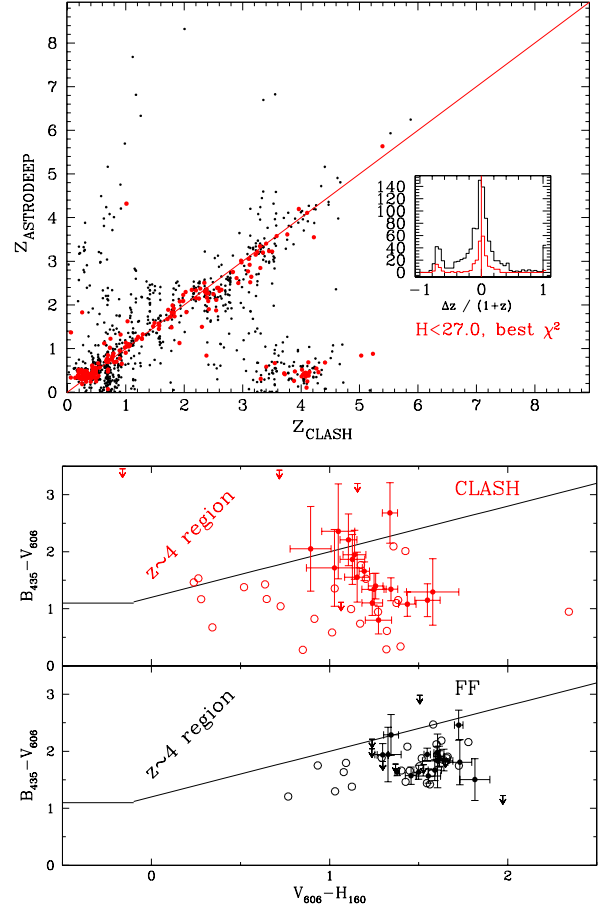
Fig. 5. *Top*: comparison between photometric redshifts from our catalogues and those from CLASH. Red points indicate bright objects with single-peaked reliable photo-z solution, according to the CLASH team (see text for details). *Bottom*: position in the $(B-V)-(V-H)$ $z \sim 4$ selection diagram of objects with $3.5 < z_{\rm CLASH} < 4.5$ and $z_{\rm ASTRODEEP} < 1$. CLASH photometry is shown in red, photometry from the Astrodeep catalogue in black. Filled circles with errorbars represent the bright sample with reliable, single-peaked CLASH photo-z.

P.Is Williams (e.g. Grillo et al. 2015), Bradač (e.g. Bradač et al. 2009) and Merten (e.g. Merten et al. 2011) do not assume that cluster mass is traced by its member galaxies and are instead solely constrained by lensing observables. Each team has provided shear and mass surface density maps. A detailed description of different models can be found on the FF website[5] and references therein. Among the available maps only the Merten ones also cover the parallel pointings of the fields under analysis. As a first step, we rebin the available shear and mass surface-density maps to match the HST dataset pixel grid to accurately assign to each galaxy a shear (γ) and mass surface-density (κ) value, computed as the average in a window of 5×5 pixels around its centroid. We then compute magnification as

$$\mu = \frac{1}{(1 - \kappa \cdot D_{zl-zp})^2 - (\gamma \cdot D_{zl-zp})^2}, \qquad (1)$$

where $D_{zl-zp} = DA(z_L, z_{\rm phot})/DA(0, z_{\rm phot})$, $DA(0, z)$ being the angular diameter distance to redshift z, $z_{\rm phot}$ the photometric redshift of the source, and z_L the redshift of the lensing cluster. Finally, in the case of the cluster pointings where eight different
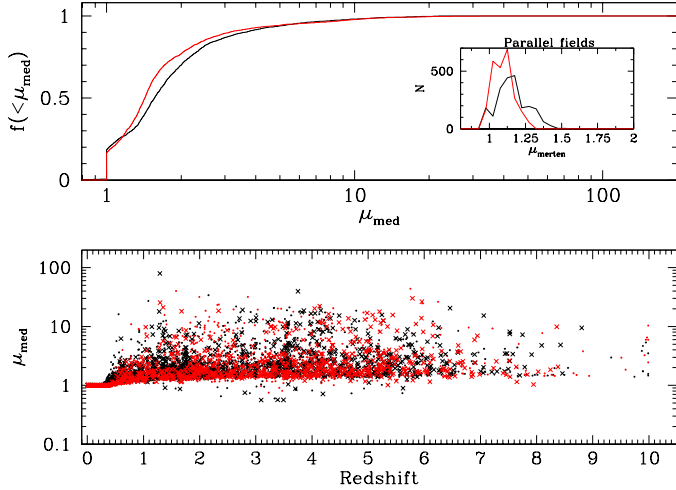
Fig. 6. *Top panel*: cumulative distribution of the median magnification (μ_{med}) values of objects in the A2744 (black) and M0416 (red) cluster fields. The *inset* shows the distribution of magnification values of objects in the two parallel fields according to the Merten et al. lens model. *Bottom panel*: μ_{med} as a function of redshift for sources in the two fields. *H*-detected and IR-detected objects are drawn as filled circles and crosses, respectively.
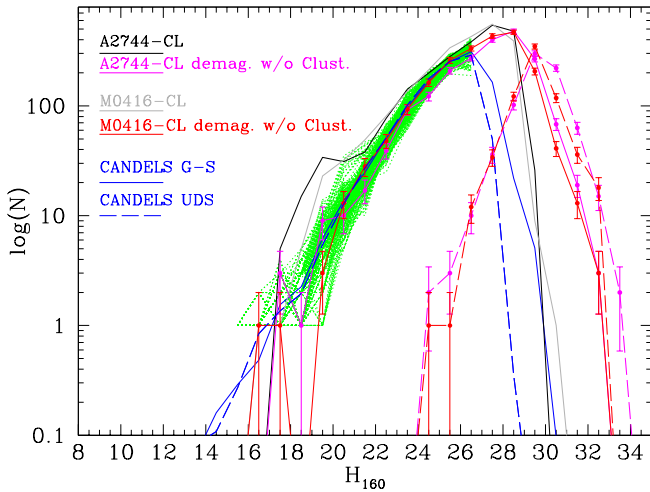

Fig. 7. Demagnified (median magnification, see text for details) *H*160 number counts in the cluster fields. Magenta and red continuous curves refer to A2744 and M0416 *H*-detected sources respectively after excluding all objects with photo-*z* consistent with the redshift of the clusters. Magenta and red dashed lines show the demagnified number counts of additional IR-detected sources (with $S/N(H160) > 1$) in each field. As a comparison, number counts normalized to the FF area from the public CANDELS GOODS-South (Guo et al. 2013) and UDS (Galametz et al. 2013) catalogues are shown as continuous and dashed blue lines, respectively. The green lines are number counts from randomly chosen portions of the CANDELS GOODS-South and UDS field, having the same area as the FF pointings.

models are available, we compute a median magnification μ_{med} to take into account model-to-model variations of the lensing maps while excluding possible outlier values. The μ_{med} values as a function of redshifts and its cumulative distributions for sources in the two cluster fields are shown in Fig. 6. As expected, the magnification in the blank fields that were computed from the Merten model is almost constant and typically low, but not negligible, with median values of 15% and 9% in A2744-Parallel and M0416-Parallel, respectively (see inset of Fig. 6, top panel). The demagnified number counts are shown in Figs. 7
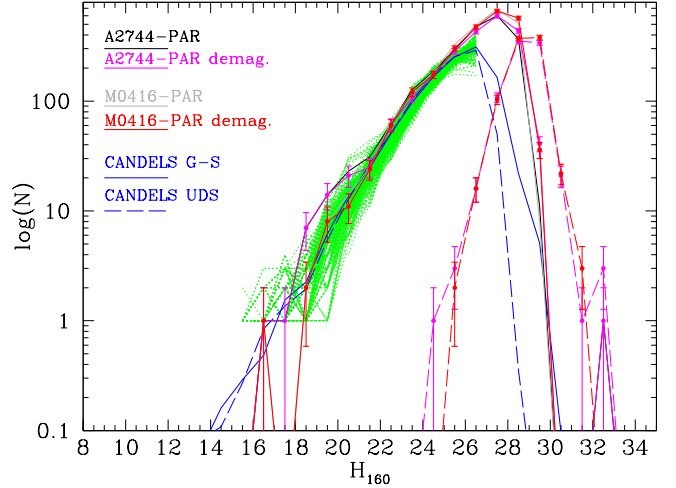

Fig. 8. Same as Fig. 7 for the A2744 and M0416 parallel fields.

and 8 for the cluster and parallel pointings, respectively, compared with both the total number counts normalized to the FF area from the CANDELS GOODS-South (Guo et al. 2013) and UDS (Galametz et al. 2013) surveys, and with number counts from randomly chosen portions of the CANDELS fields having the same area as the FF pointings. At bright magnitudes, the FF number counts are consistent with the CANDELS ones once magnification is taken into account and, in the case of the cluster pointings, sources with redshift that are compatible with being members of the A2744 and M0416 clusters (z_{phot} within $\Delta z = 0.1$ from the cluster redshift) are removed. At faint magnitudes the Frontier Fields cluster pointings allow us to detect sources that are up to ~3–4 mag intrinsically fainter than objects in the deepest areas of the CANDELS fields.

5. Rest-frame physical properties

The ultra deep IR observations of the FF, in combination with the strong gravitational lensing effect allows stellar masses and star-formation rates to be probed at unprecedented limits. In Fig. 9, we show the de-magnified M_{star} and star formation rates (SFRs) as a function of redshift for galaxies in the two cluster fields compared to the sample from CANDELS GOODS-South, among the most studied "wide" fields for investigating these properties at high-*z*. Intrinsic M_{star} and SFR are obtained by correcting the estimates derived through SED-fitting on observed magnitudes (Sect. 3), considering its μ_{med} value for each source. We derive the mass completeness limits using the procedure presented in Fontana et al. (2004), which is based on the measurement of the actual distribution of the M_{star}/L as a function of redshift to derive limiting stellar mass beyond the flux limit. We base our computation on the M_{star}/L distributions derived by Grazian et al. (2015) from GOODS-South that provides a large and deep enough (after the inclusion of the HUDF) sample for this purpose. The strict completeness limit, which corresponds to $H = 27.25$ (90% detection completeness for $R_h = 0.2$ arcsec disks in the FF), is shown as a continuous blue line, the dashed one corresponding to galaxies magnified by a factor $\mu = 10$. These "maximally old limits" (MOL) are derived by considering the model with the lowest M_{star}/L in our synthetic library, i.e. maximally old galaxies with formation redshift $z = 20$, a declining star formation history ($\tau = 0.1$ Gyr), $E(B - V) = 0.1$, and $Z = 0.2 Z_{\odot}$. Clearly, the observed sample reaches lower M_{star} values for less extreme galaxy populations: we show as continuous
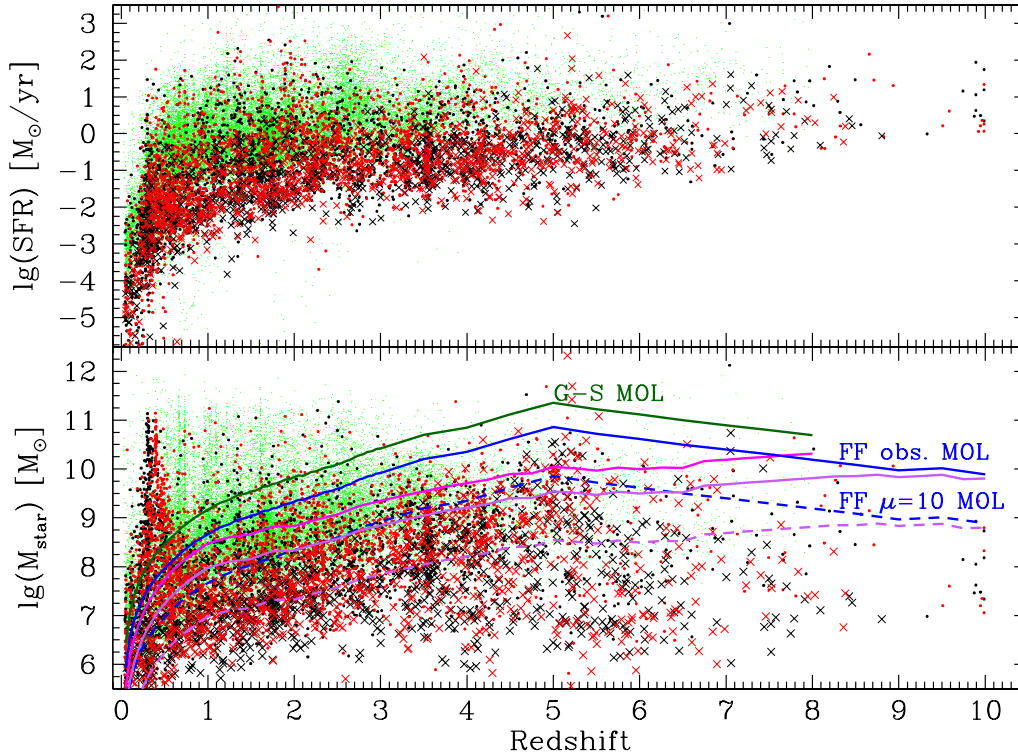
Fig. 9. *Top panel*: demagnified SFR as a function of redshift in the A2744 (black) and M0416 (red) clusters. Filled circles and crosses refer to *H*-detected and IR-detected sources respectively. For reference SFRs of objects from the CANDELS GOODS-South field are shown as green dots. *Bottom panel*: demagnified stellar masses, same symbols as above. The continuous and dashed blue lines show the limiting M_{star} for a "maximally old model" at $H160 = 27.25$ (observed 90% completeness limit) and $H160 = 29.75$ (90% completeness limit for $\mu = 10$). The continuous and dashed lines show the corresponding "completeness corrected" limiting M_{star} (see text for details). The dark green and magenta continuous lines show the "maximally old" and completeness-corrected limiting M_{star} of CANDELS GOODS-South from Grazian et al. (2015).

(observed limit) and dashed (for the case of $\mu = 10$) purple lines the mass limits at which a completeness correction factor that is lower than 1.5 needs to be applied by taking into account the appropriate M_{star}/L distribution (see Fontana et al. 2004, for a detailed description of the procedure). A comparison with the corresponding MOL and "completeness corrected" limits for the GOODS-South Wide field ($H160_{lim} = 26.0$) taken from Grazian et al. (2015) shows that the Frontier Fields clusters allow us to probe the galaxy stellar mass distribution at 0.5–1.5 dex lower masses, depending on the magnification, with respect to GOODS. The inclusion of the addtional sample of IR-detected objects yields sources at M_{star} as low as 10^7–10^8 at high-z, although a formal derivation of completeness limits is not straightforward in this case. As shown in the top panel of Fig. 9, the Frontier Fields also allow to probe high-z galaxies at intrinsic SFRs > 1 dex lower than in the wide GOODS-South area, reaching 0.1–1 M_{star}/yr at $z \sim 6$–10.

6. Summary and conclusions

We have presented a public release of photometric redshifts and rest-frame galaxy properties from multiwavelength photometry of the Frontier Fields Abell-2744 and MACS-J0416 cluster and parallel pointings, including HST, deep *K*-band and *Spitzer* data, as described in the companion paper, Merlin et al. (2016). We have derived photometric redshifts as the median among six different estimates coming from a variety of codes and approaches (Sect. 2). Their typical accuracy, as defined from the semi-interquartile range of the different measurements, goes from 0.05 to 0.3 at bright and faint magnitudes, respectively, with less

than 10% of sources having SIQR > 1 at $H < 26$, and about 20% at $H \sim 29$. A comparison with available spectroscopic samples consistently shows a $\sigma_{\Delta z/(1+z)} \sim 0.04$ with 7–10% of outliers. We find that the most important factor limiting the accuracy of photometric redshifts in the FF is the relatively low number of filters available compared to other surveys, which means that extending the FF spectral coverage is the most promising way to improve accuracy in photometric redshifts and derived quantities. We have determined magnification values from all available lensing models on an object-by-object basis, taking into account source positions and redshifts. The resulting demagnified number counts (Sect. 4) are perfectly consistent with number counts from the CANDELS fields at the bright end, while reaching out to an intrinsic $H \gtrsim 32$. We have shown that the Frontier Fields survey enables us to detect objects with stellar mass $M_{star} \sim 10^7$–10^8 $M_\odot$ and intrinsic SFRs ~ 0.1–1 $M_\odot$/yr at $z > 5$ (Sect. 5). Photometric redshifts, magnification values, rest-frame properties, and supporting information are all made publicly available as described in the Appendix.

References

Arnouts, S., Cristiani, S., Moscardini, L., et al. 1999, MNRAS, 310, 540
Atek, H., Richard, J., Kneib, J.-P., et al. 2015, ApJ, 800, 18
Balestra, I., Mercurio, A., Sartoris, B., et al. 2016, ApJS, submitted
    [arXiv:1511.02522]
Barden, M., Häußler, B., Peng, C. Y., McIntosh, D. H., & Guo, Y. 2012,
    MNRAS, 422, 449
Bertin, E., & Arnouts, S. 1996, A&AS, 117, 393
Blanton, M. R., & Roweis, S. 2007, AJ, 133, 734
Bradač, M., Treu, T., Applegate, D., et al. 2009, ApJ, 706, 1201
Brammer, G. B., van Dokkum, P. G., & Coppi, P. 2008, ApJ, 686, 1503
Bruzual, G., & Charlot, S. 2003, MNRAS, 344, 1000
Calzetti, D., Armus, L., Bohlin, R. C., et al. 2000, ApJ, 533, 682
Castellano, M., Fontana, A., Grazian, A., et al. 2012, A&A, 540, A39
Castellano, M., Sommariva, V., Fontana, A., et al. 2014, A&A, 566, A19
Christensen, L., Richard, J., Hjorth, J., et al. 2012, MNRAS, 427, 1953
Coe, D., Bradley, L., & Zitrin, A. 2015, ApJ, 800, 84
Dahlen, T., Mobasher, B., Faber, S. M., et al. 2013, ApJ, 775, 93
Ebeling, H., Ma, C.-J., & Barrett, E. 2014, ApJS, 211, 21
Fan, X., Strauss, M. A., Becker, R. H., et al. 2006, AJ, 132, 117
Fioc, M., & Rocca-Volmerange, B. 1997, A&A, 326, 950
Fontana, A., D'Odorico, S., Poli, F., et al. 2000, AJ, 120, 2206
Fontana, A., Pozzetti, L., Donnarumma, I., et al. 2004, A&A, 424, 23
Galametz, A., Grazian, A., Fontana, A., et al. 2013, ApJS, 206, 10
Giallongo, E., Menci, N., Grazian, A., et al. 2014, ApJ, 781, 24
Grazian, A., Fontana, A., de Santis, C., et al. 2006, A&A, 449, 951
Grazian, A., Fontana, A., Santini, P., et al. 2015, A&A, 575, A96
Grillo, C., Suyu, S. H., Rosati, P., et al. 2015, ApJ, 800, 38
Guo, Y., Ferguson, H. C., Giavalisco, M., et al. 2013, ApJS, 207, 24
Ilbert, O., Arnouts, S., McCracken, H. J., et al. 2006, A&A, 457, 841
Ilbert, O., Capak, P., Salvato, M., et al. 2009, ApJ, 690, 1236
Ishigaki, M., Kawamata, R., Ouchi, M., et al. 2015, ApJ, 799, 12
Jauzac, M., Clément, B., Limousin, M., et al. 2014, MNRAS, 443, 1549
Johnson, T. L., Sharon, K., Bayliss, M. B., et al. 2014, ApJ, 797, 48
Jouvel, S., Host, O., Lahav, O., et al. 2014, A&A, 562, A86
Laporte, N., Streblyanska, A., Clement, B., et al. 2014, A&A, 562, L8
Laporte, N., Streblyanska, A., Kim, S., et al. 2015, A&A, 575, A92
McLeod, D. J., McLure, R. J., Dunlop, J. S., et al. 2015, MNRAS, 450, 3032
McLure, R. J., Dunlop, J. S., de Ravel, L., et al. 2011, MNRAS, 418, 2074
Merlin, E., Fontana, A., Ferguson, H. C., et al. 2015, A&A, 582, A15
Merlin, E., Amorìn, R., Castellano, M., et al. 2016, A&A, 590, A30
Merten, J., Coe, D., Dupke, R., et al. 2011, MNRAS, 417, 333
Mobasher, B., Dahlen, T., Ferguson, H. C., et al. 2015, ApJ, 808, 101
Oesch, P. A., Bouwens, R. J., Illingworth, G. D., et al. 2015, ApJ, 808, 104
Oguri, M. 2010, PASJ, 62, 1017
Owers, M. S., Randall, S. W., Nulsen, P. E. J., et al. 2011, ApJ, 728, 27
Peng, C. Y., Ho, L. C., Impey, C. D., & Rix, H.-W. 2010, AJ, 139, 2097
Postman, M., Coe, D., Ford, H., et al. 2011, in BAAS, 43, AAS Meet. Abstr. 217,
    227.06
Prevot, M. L., Lequeux, J., Prevot, L., Maurice, E., & Rocca-Volmerange, B.
    1984, A&A, 132, 389
Rosati, P., Balestra, I., Grillo, C., et al. 2014, The Messenger, 158, 48
Salpeter, E. E. 1955, ApJ, 121, 161
Santini, P., Ferguson, H. C., Fontana, A., et al. 2015, ApJ, 801, 97
Schaerer, D., & de Barros, S. 2009, A&A, 502, 423
Schlegel, D. J., Finkbeiner, D. P., & Davis, M. 1998, ApJ, 500, 525
Skelton, R. E., Whitaker, K. E., Momcheva, I. G., et al. 2014, ApJS, 214, 24
Treu, T., Schmidt, K. B., Brammer, G. B., et al. 2015, ApJ, 812, 114
Wang, X., Hoag, A., Huang, K., et al. 2015, ApJ, 811, 29
Zheng, W., Shu, X., Moustakas, J., et al. 2014, ApJ, 795, 93
Zitrin, A., Meneghetti, M., Umetsu, K., et al. 2013, ApJ, 762, L30
Zitrin, A., Zheng, W., Broadhurst, T., et al. 2014, ApJ, 793, L12

Appendix A: Released catalogues

All the catalogues and derived quantities described in this paper are publicly released and can be downloaded from the ASTRODEEP website at http://www.astrodeep.eu/frontier-fields/. The catalogues and images can be browsed from a dedicated interface at http://astrodeep.u-strasbg.fr/ff/index.html

Photometric redshift catalogues contain the following information:

- ID: identification number in the input photometric catalogues from M16. The IR-detected objects have ID = 20000 + their original ID in the relevant detection catalogues and segmentation maps.
- ZBEST: corresponds to the reference (median) photo-z value, except when a match with a publicly available high-quality spectroscopic source is found within 1 arcsec. Sources for which the photo-z run did not converge to a solution are set to ZBEST = −1.0.
- ZBEST_SIQR: median photometric redshift uncertainty range (equal to 0 for spectroscopic sources).
- MAGNIF: median magnification (cluster fields) or magnification from the Merten model (parallel fields).
- ZSPECFLAG: the value is set = 1 for sources with spectroscopic redshift, = 0 otherwise.
- ZSPECID: identification number of spectroscopic counterpart from public catalogues.
    For A2744 the following convention is used: sources from Owers et al. (2011) have ZSPECID equal to the row index in the original file; sources from Johnson et al. (2014) have ZSPECID equal to 3000 + row index from Table 2 in the paper, objects from the GLASS survey have ZSPECID = 10000 + original ID.
    For MACS0416 the following convention is used: sources from Ebeling et al. (2014) have ZSPECID equal to the original ID; the strongly lensed galaxies made available by STSci for FF lensing modelling (from Grillo et al. 2015; Christensen et al. 2012) have ZSPECID = 3000 + row index from the original file, objects from the GLASS survey have ZSPECID = 10000 + original ID.
    The value is −1 for sources with no spectroscopic counterpart.
- Chi2: χ^2 of the SED-fitting with stellar only templates at redshift fixed to ZBEST.
- MSTAR, MSTAR_MIN, MSTAR_MAX: stellar mass in units of 10^9 $M_\odot$ (assuming Salpeter IMF) and relevant uncertainty range. Uncertainties on physical parameters are defined from the range where $P(\chi^2) > 32\%$ estimated in a $\Delta z = 0.2$ redshift bin around the reference photometric redshift.
- SFR, SFR_MIN, SFR_MAX: star formation rate ($M_\odot$/yr) and relevant uncertainty range.
- Chi2_NEB: χ^2 of the SED-fitting with stellar plus nebular models at redshift fixed to ZBEST.
- MSTAR_NEB, MSTAR_MIN_NEB, MSTAR_MAX_NEB: stellar mass (10^9 $M_\odot$) estimated from stellar plus nebular fits.
- SFR_NEB, SFR_MIN_NEB, SFR_MAX_NEB: star formation rate ($M_\odot$/yr) estimated from the stellar plus nebular fits.
- RELFLAG: This flag is meant to provide a combined indication of the robustness of photometric and photo-z estimates. Sources with RELFLAG=1 have enough reliable photometric information to estimate photometric-redshifts. Instead, the value is =0 for sources either: falling close to the border of the images; close to strong residual features of the Galfit image pre-processing; found to be spurious (mostly stellar spikes) from visual inspection; having SExtractor FLAG > =16; having unphysical flux in the detection band; having less than five HST bands with reliable flux measurement available for photo-z procedures.